EUROPEAN COOPERATION IN SCIENCE & TECHNOLOGY

Report on the outcomes of a Short-Term Scientific Mission

Action number: CA24157

Grantee name: Sourav Kumar Sahoo

Details of the STSM

Title: Quantitative Geophysical Field Inversion for Permafrost Monitoring using laboratory experiment.

Start and end date: 13/08/2026 to 31/08/2026

Host: Prof. Hansruedi Maurer, ETH Zürich

Additional scientific visit: Prof. Christian Hauck, University of Fribourg

Description of the work carried out during the STSM

Description of the activities carried out during the STSM. Any deviations from the initial working plan shall also be described in this section.

The STSM was hosted by Prof. Hansruedi Maurer at ETH Zürich and focused on improving the link between laboratory geophysical calibration, field-scale permafrost monitoring and petrophysical joint inversion. Activities included technical discussions at ETH Zürich, visits to the ETH acoustics laboratory and Bedretto Underground Laboratory, and a visit to Prof. Christian Hauck at the University of Fribourg.

First, existing four-phase and petrophysical joint-inversion workflows were assessed to identify where laboratory calibration could most effectively reduce uncertainty in estimates of water, ice, air and rock content. The review considered porosity, rock-frame and phase velocities, pore-water resistivity, Archie cementation and saturation exponents, geometric-mean phase resistivities, phase partitioning, data errors, regularisation, prior constraints and ice-rock ambiguity. A parameter-sensitivity and uncertainty table was produced, ranking porosity, rock-frame velocity, pore-water resistivity, Archie parameters, rock and ice resistivities, electrical mixing model, sample heterogeneity and data weighting as high priorities for laboratory or numerical evaluation. This is just the initial assessment and detailed analysis will be carried out later using open-source Python-based code, pyGIMLi.

Second, practical guidance was developed for designing laboratory measurements that are relevant to field acquisition. The guidance recommends matching laboratory frequencies as closely as practical to field bandwidths, or measuring several frequencies to quantify dispersion; controlling temperature, salinity, saturation and freeze-thaw or hydrate history; recording total and connected porosity; and using representative sample dimensions. Electrical measurements should use documented electrode geometry, stable contact resistance and reciprocal or repeat measurements. Elastic measurements should use repeatable transducer loading and coupling, consistent propagation paths and uncertainty estimates. Where possible, electrical and elastic data should be acquired on the same specimen and at the same state. Large boulders, mixed grain sizes and connected voids cannot be represented by one small specimen, so multi-scale tests and synthetic heterogeneous models are required. The main concern is reproducing field-scale heterogeneity in the laboratory; preserving representative cores is an additional challenge. A suitable middle path is therefore to prepare a series of synthetic laboratory samples that vary field-relevant properties such as lithology, ice content and grain-size distribution. These laboratory measurements can then be used to calibrate the models before applying the calibrated relationships to field-data inversion. We have developed a joint PhD proposal on this topic of permafrost ice content quantification, which is now advertised in Southampton.

Third, a first-order joint elastic-electrical inversion was developed for an existing methane-hydrate-bearing Berea sandstone dataset. Elastic wave velocity, attenuation and resistivity observations were used for jointly inverting for permeability changes during hydrate formation. The results were compared with previously published elastic-only and electrical-only estimates of permeability changes (Sahoo and Best 2021).

Description of the STSM main achievements and planned follow-up activities

The STSM achieved the three planned outcomes and strengthened collaboration between laboratory rock physics, underground geophysics, field permafrost monitoring and petrophysical inversion.

The first achievement was a literature-supported calibration and uncertainty framework. It identifies which fixed or weakly constrained quantities most strongly influence recovered phase fractions and which can be measured in the laboratory. Porosity, rock-frame velocity, pore-water resistivity, Archie cementation and saturation exponents, rock and ice resistivities, electrical mixing-law choice, sample scale and data weighting were assigned the highest priority. Ice-rock ambiguity and non-unique phase partitioning were identified as limitations that require combined measurements, realistic uncertainty estimates and numerical testing rather than calibration of a single parameter.

The second achievement was a practical laboratory-measurement guidance. The recommended workflow is to define the field target and acquisition bandwidth first; select representative materials and scales; measure baseline dry, saturated and frozen states; vary temperature, salinity and phase saturation in controlled steps; acquire electrical and elastic data on the same specimen and state; document electrode and transducer geometry, contact and coupling; repeat measurements to quantify uncertainty; and test whether calibrated relationships remain valid across scales. The principal do’s are to preserve consistent sample state, measure pore-fluid properties directly, report acquisition frequency and geometry, use replicates and include heterogeneity in the experimental design. The principal don’ts are to transfer one

parameter set between contrasting landforms, assume laboratory and field frequencies are equivalent, infer ice from high resistivity alone, ignore unfrozen water or coexisting gas, or apply Archie and geometric-mean models without testing their assumptions.

The third achievement was a proof-of-concept balanced joint inversion using the existing hydrate-bearing sandstone dataset. The joint solution reproduces the broad increase in shear-wave velocity and resistivity and the overall decrease in relative permeability with increasing hydrate saturation. The joint estimate generally lies between, or close to, the separate elastic and electrical estimates. Residual analysis shows that the largest mismatches occur in the elastic data at approximately 25–26% hydrate saturation, where one shared permeability does not fully reproduce the sharp attenuation decrease and velocity increase. This identifies a clear target for morphology-dependent modelling and parameter refinement.

Follow-up work will implement systematic pyGIMLi sensitivity tests, vary the highest-priority parameters, compare Archie and geometric-mean formulations, examine boulder-scale heterogeneity and field-to-laboratory scaling, and test morphology-dependent or regularised joint inversion. The work supports CA24157 by improving quantitative interpretation of complementary geophysical observations and provides a basis for continued collaboration and a potential publication. We have developed a joint PhD proposal on permafrost ice quantification and submitted to the University of Southampton for the 2027 intake. This will support CA24157 by training students.

1. SUPPORTING TECHNICAL ANNEXES

The annexes consolidate the three technical outcomes supporting the two official summary sections above.

2. ANNEX A. LABORATORY-CALIBRATION ASSESSMENT AND SENSITIVITY TABLE

This table identifies the parameters and modelling choices that most strongly affect four-phase joint inversion and indicates where laboratory calibration or numerical testing can reduce uncertainty.

Parameter or issue	Main uncertainty	Laboratory or numerical test	Priority
Porosity	Field-scale porosity may include large voids between boulders and may not match laboratory porosity	Measure total and connected porosity at different sample scales	High
Rock-frame velocity	Depends on lithology, cracks, porosity, pressure, temperature, and consolidation	Measure dry, saturated, and frozen samples; test a range around the published value	High
Water velocity	May vary with temperature and salinity	Measure or calculate for the actual pore fluid	Medium
Ice velocity	Affected by temperature, impurities, cracks, and brine	Measure frozen samples under controlled conditions	Medium to high
Air velocity	Usually small compared with other uncertainties	Retain as a fixed baseline and test only if needed	Low
Pore-water resistivity	Strongly affected by temperature, salinity, and solute concentration during freezing	Measure across temperature and salinity ranges	High
Cementation exponent	Depends on pore geometry and connectivity	Fit using samples with known porosity at full water saturation	High
Saturation exponent	Depends on saturation history, phase distribution, and pore structure	Fit using controlled water, ice, and air saturations	High
Rock resistivity	Lithology-, moisture-, crack-, and temperature-dependent	Measure representative rocks and sediments	High

Ice resistivity	Sensitive to temperature, salinity, impurities, and unfrozen water	Measure frozen samples over representative conditions	High
Air resistivity	Air is theoretically extremely resistive, but numerical values affect convergence	Test logarithmically spaced values in pyGIMLi	Medium
Electrical mixing model	Different models may recover different phase fractions	Compare both models against samples of known composition	High
Phase partitioning	Different phase combinations may produce similar geophysical responses	Test recovery using synthetic models with known fractions	High
Ice-rock ambiguity	Ice and rock are both electrically resistive and may be difficult to separate	Test rock-ice mixtures using combined velocity and resistivity	High
Sample heterogeneity and scale	Small samples may not represent boulders, large voids, or mixed field materials	Test different particle sizes, sample sizes, and synthetic boulder models	High
Data errors and weighting	One dataset may dominate if errors are not represented correctly	Use repeatability errors and numerical weighting tests	High
Regularisation and priors	Strong settings may suppress real contrasts; weak settings may amplify artefacts	Test systematically in pyGIMLi	High

3. ANNEX B. PRACTICAL LABORATORY GUIDANCE

The guidance translates the sensitivity assessment and discussions during the laboratory and field visits into a practical measurement workflow.

Topic	Recommended practice	Do	Do not
Frequency and scaling	Measure at several frequencies spanning the accessible laboratory band; report bandwidth and dispersion; compare trends rather than assuming direct equivalence with field frequencies.	Match acquisition settings where practical and quantify frequency dependence.	Use a single high-frequency laboratory value as a field-scale constant.

Temperature and phase state	Control and log specimen temperature, equilibration time, freeze-thaw or hydrate history, and unfrozen-water conditions.	Wait for thermal and electrical stability before each measurement.	Treat nominal chamber temperature as the internal sample temperature without verification.
Salinity and pore fluid	Measure pore-water conductivity or resistivity at the test temperature and track concentration changes caused by freezing or hydrate formation.	Use the actual pore fluid in the petrophysical model.	Assume room-temperature water resistivity remains valid throughout the test.
Saturation control	Determine water, ice or hydrate, gas and air fractions independently where possible using mass balance, pressure-temperature calculations or imaging.	Create repeatable saturation steps and retain uncertainty bounds.	Infer ice or hydrate from high resistivity alone.
Sample geometry and scale	Use specimens large enough to contain representative grains and pores; test more than one size where heterogeneity is important.	Report dimensions, orientation and representativeness.	Generalise from one small homogeneous specimen to boulder-rich field material.
Electrical setup	Document electrode number, spacing, area and configuration; monitor contact resistance; use reciprocal and repeated readings.	Keep wiring, current level and electrode contact consistent.	Change electrode geometry between states without accounting for the change.
Elastic setup	Document transducer type, centre frequency, coupling, loading	Repeat coupling tests and propagate picking uncertainty.	Interpret changes caused by coupling

	and propagation path; use identical picking and attenuation processing.		or load as material response.
Joint acquisition	Acquire elastic and electrical measurements on the same specimen, at the same temperature and phase state, preferably within one stabilised measurement sequence.	Synchronise metadata and use common sample-state identifiers.	Combine observations from unmatched states without an explicit matching criterion.
Uncertainty and QA	Use replicate tests, reference states, calibration standards and error propagation; retain raw and processed data.	Weight datasets using measured repeatability and model uncertainty.	Allow the dataset with more observations or smaller nominal error to dominate automatically.
Model selection	Test Archie and geometric-mean formulations against specimens with independently known composition.	State assumptions and compare model residuals and recovered fractions.	Select a mixing law only because it converges or gives plausible fractions.
Heterogeneity and upscaling	Combine core tests, larger physical models, imaging and synthetic boulder or void models.	Report the scale over which calibrated parameters are valid.	Assume a single effective parameter set applies to all landforms and scales.

4. ANNEX C. JOINT ELASTIC-ELECTRICAL INVERSION DEMONSTRATION

C.1 Objective and relationship to the published analyses

A proof-of-concept joint inversion was developed for the existing Cycle 3 methane-hydrate experiment on Berea sandstone. The experimental measurements, thermodynamic phase fractions and hydrate-morphology interpretation were reported previously by Sahoo et al. (2018a, 2018b). Sahoo and Best (2021) subsequently estimated relative permeability independently from shear-wave velocity and attenuation and from electrical resistivity. The new contribution was to fit the elastic

and electrical observations simultaneously using one shared relative permeability. Thus, the workflow can be summarised as:

$$\Delta V_S, \quad \Delta Q_S^{-1}, \quad R_t \longrightarrow k_{\text{rel}}^{\text{joint}}$$

where ΔV_s is the change in shear-wave velocity, ΔQ_s^{-1} is the change in inverse shear-wave quality factor, R_t is the measured bulk resistivity and k_{rel} is relative permeability. The demonstration does not repeat the published data acquisition or separate inversions. It combines their forward relationships within a common objective function.

C.2 Experimental dataset and matched observations

Cycle 3 was selected because elastic and electrical observations were available over the hydrate-formation sequence. The Berea sandstone specimen had a porosity of 0.22, an initial permeability of 448 mD, a diameter of 4.97 cm and a length of 2.06 cm. The initial water saturation was 83.5%, the brine concentration was 35 g L^{-1} NaCl, the differential pressure was 55 MPa and the elastic measurements used here were evaluated at 648 kHz. Hydrate, water and gas saturations had been calculated independently from the measured pressure-temperature history.

Electrical measurements were less frequent than elastic measurements. Resistivity observations therefore defined the joint-inversion points, and the closest elastic observation was selected using hydrate saturation stored in column 50 of both datasets:

$$S_h^{\text{electrical}} = \text{res}(:,50), \qquad S_h^{\text{elastic}} = \text{s2f}(:,50)$$

$$\Delta S_h = \left| S_h^{\text{electrical}} - S_h^{\text{elastic}} \right|$$

Only matches with $\Delta S_h \leq 0.5$ percentage points were retained. If more than one resistivity observation matched the same elastic row, the pair with the smallest saturation difference was used. This avoided interpolating resistivity across large temporal gaps and produced a common table containing hydrate and water saturation, V_s, Q_s^{-1}, resistivity, temperature, pore pressure, density and original row indices.

C.3 Inversion parameter and bounds

The common inversion parameter was relative permeability, defined by:

$$k_{\text{rel}} = \frac{k_{\text{eff}}}{k_0}$$

where k_e is the effective permeability of the hydrate-bearing specimen and k_0 is the permeability of the hydrate-free host. Optimisation was performed in logarithmic space:

$$x = \log_{10}(k_{\text{rel}}), \qquad k_{\text{rel}} = 10^x$$

C.4 Elastic forward model

The published two-phase and three-phase Biot-type poroelastic models and their physical parameters were retained. The two-phase formulation represented low hydrate saturation, where hydrate behaved mainly as part of the pore filling. The three-phase formulation represented higher saturation, where an interconnected hydrate framework contributed as an additional solid phase. For each trial permeability, the model returned changes relative to the reference observation:

$$\Delta V_S^{\text{pred}} = V_S^{\text{pred}}(S_h) - V_S^{\text{pred}}(S_{h,\text{ref}})$$

$$\Delta Q_S^{-1,\text{pred}} = Q_S^{-1,\text{pred}}(S_h) - Q_S^{-1,\text{pred}}(S_{h,\text{ref}})$$

Using changes rather than absolute values retained consistency with the earlier elastic inversion and reduced sensitivity to fixed reference offsets. The model contains permeability-dependent viscous interactions among the sediment frame, hydrate framework and pore fluid. The published interpretation associates changes near approximately 6% and 20% hydrate saturation with transitions from pore-floating hydrate to pore bridging and then to an inter-pore hydrate framework (Sahoo et al., 2018a; Sahoo and Best, 2021).

C.5 Electrical forward model

The earlier Archie-based permeability relationship was rearranged so that the joint inversion predicted measured resistivity directly from each trial relative permeability:

$$R_t^{\text{pred}} = \frac{a\,\phi^{-m} R_w}{k_{\text{rel}}} \left(\frac{S_w - S_{\text{wir}}}{1 - S_{\text{wir}}} \right)$$

Here a = 1 is the Archie coefficient, φ = 0.22 is porosity, m = 3.1 is the cementation exponent, Rw is brine resistivity, Sw is water saturation and Swir = 0.23 is irreducible water saturation. Salt excluded during hydrate formation increases the concentration of the remaining brine. The concentration and temperature corrections were represented as:

$$C_{\text{NaCl}}(S_w) = C_{\text{NaCl},0} \frac{S_{w,0}}{S_w}$$

$$C_w(T) = C_w(25)[1 + \alpha_C(T - 25)], \qquad \alpha_C = 0.019\ ^\circ\text{C}^{-1}$$

$$R_w = \frac{1}{C_w}$$

This formulation fitted observed resistivity rather than treating independently derived electrical permeability as a prior. It also retained the salinity and temperature corrections used in the published electrical interpretation.

C.6 Error-normalised residuals

The three observables have different units, scales and uncertainties. They were therefore combined using dimensionless residuals:

$$r_{V_S} = \frac{\Delta V_S^{\mathrm{obs}} - \Delta V_S^{\mathrm{pred}}}{\sigma_{\Delta V_S}}$$

$$r_{Q_S^{-1}} = \frac{\Delta Q_S^{-1,\,\mathrm{obs}} - \Delta Q_S^{-1,\,\mathrm{pred}}}{\sigma_{\Delta Q_S^{-1}}}$$

$$r_R = \frac{\ln R_t^{\mathrm{obs}} - \ln R_t^{\mathrm{pred}}}{\sigma_{\ln R}}$$

The shear-wave velocity uncertainty was approximately 0.3%. Because elastic changes were calculated relative to a reference observation, uncertainties in the selected and reference measurements were propagated in quadrature:

$$\sigma_{\Delta V_S} = \sqrt{\sigma_{V_S,\,i}^2 + \sigma_{V_S,\,\mathrm{ref}}^2}, \qquad \sigma_{\Delta Q_S^{-1}} = \sqrt{\sigma_{Q_S^{-1},\,i}^2 + \sigma_{Q_S^{-1},\,\mathrm{ref}}^2}$$

Logarithmic resistivity was used because resistivity is positive and spans a wider relative range than the elastic measurements. A preliminary electrical-model uncertainty of 15% was assigned:

$$\sigma_{\ln R} = \ln(1 + 0.15)$$

This term represents not only instrumental error but also uncertainty in porosity, water saturation, cementation exponent, irreducible water saturation, salinity and temperature corrections, and the Archie-based model itself.

C.7 Balanced objective function and numerical implementation

The elastic contribution was defined as the mean of the two squared elastic residuals, whereas the electrical contribution contained the squared resistivity residual:

$$\Phi_{\mathrm{elastic}} = \frac{1}{2}\left(r_{V_S}^2 + r_{Q_S^{-1}}^2\right), \qquad \Phi_{\mathrm{electrical}} = r_R^2$$

$$\Phi_{\mathrm{joint}} = \frac{1}{2}\left[\left(\frac{\Delta V_S^{\mathrm{obs}} - \Delta V_S^{\mathrm{pred}}}{\sigma_{\Delta V_S}}\right)^2 + \left(\frac{\Delta Q_S^{-1,\,\mathrm{obs}} - \Delta Q_S^{-1,\,\mathrm{pred}}}{\sigma_{\Delta Q_S^{-1}}}\right)^2\right] + \left(\frac{\ln R_t^{\mathrm{obs}} - \ln R_t^{\mathrm{pred}}}{\sigma_{\ln R}}\right)^2$$

The factor of one half prevents the elastic dataset from receiving twice the aggregate weight merely because it contains two observables. Elastic and electrical datasets therefore have equal dataset-level influence, while each measurement remains normalised by its uncertainty. The objective was minimised independently at each matched saturation point using fminsearch, with the previous solution used as the starting model for the next point. The implementation produced elastic-only, electrical-only and balanced joint estimates together with predicted data, normalised residuals and separate objective contributions.

C.8 Results, interpretation and limitations

Figure 1 compares observed and predicted elastic and electrical responses. The joint model reproduces the broad increase in shear-wave velocity and resistivity and provides a reasonable fit near 20–23% hydrate saturation. At approximately 25–26%, however, the model underpredicts the velocity increase and does not reproduce the

sharp fall in attenuation after its maximum. Figure 2 confirms that the largest normalised residuals occur in the two elastic observables at the highest saturations. The positive velocity residual and strongly negative attenuation residual indicate a systematic model limitation rather than random scatter.

Figure 3 compares the resulting relative permeability with the separate elastic and electrical estimates. All methods show a substantial permeability reduction with increasing hydrate saturation. The balanced joint estimate generally lies between, or close to, the separate estimates, demonstrating the intended compromise between complementary constraints. Comparison with the plotted Tokyo-model curves shows that no single exponent follows all points over the complete saturation range.

The demonstration therefore establishes feasibility but does not show that one shared permeability and one fixed parameter set fully explain every morphology regime. Current limitations include fixed porosity and Archie parameters, a preliminary 15% electrical-model uncertainty, no explicit inversion for coexisting gas, independent inversion at each saturation point and no regularisation across the sequence. Follow-up work will test electrical uncertainties of 10–30%, sensitivity to φ, m and Swir, explicit gas saturation, separate morphology regimes, weak saturation-domain regularisation and balanced versus ungrouped objectives.

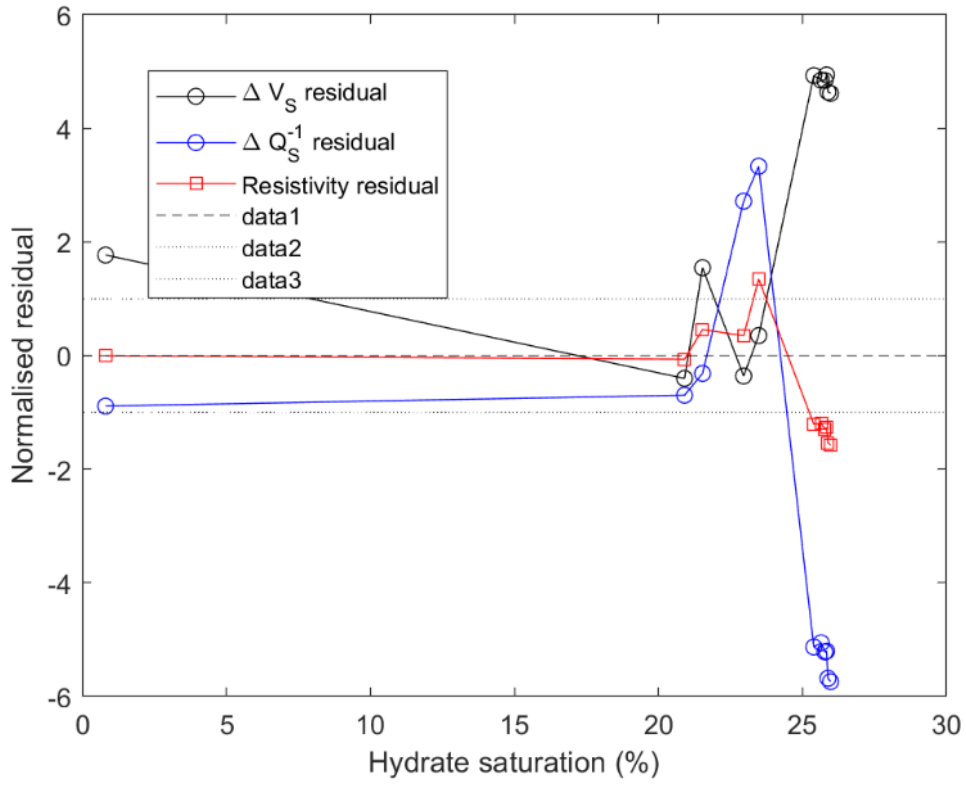

Figure 1. Observed and jointly predicted changes in shear-wave velocity, shear-wave attenuation and electrical resistivity as functions of hydrate saturation for the matched Cycle 3 observations.

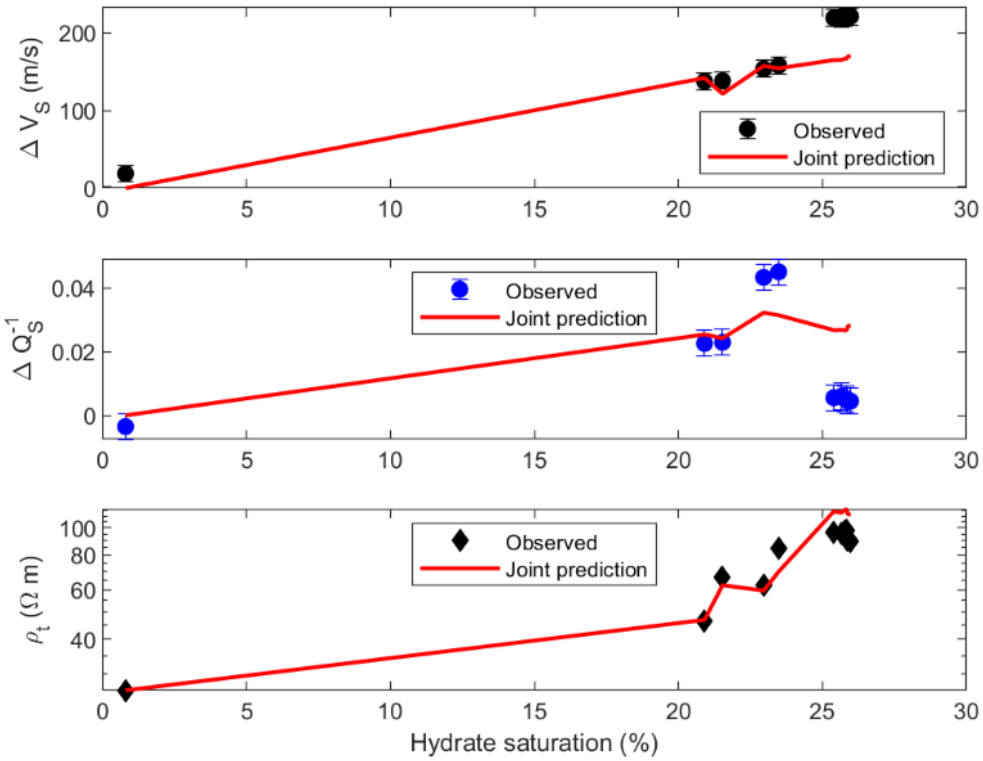

Figure 2. Normalised residuals for shear-wave velocity, shear-wave attenuation and logarithmic resistivity. The largest elastic departures occur at approximately 25–26% hydrate saturation.

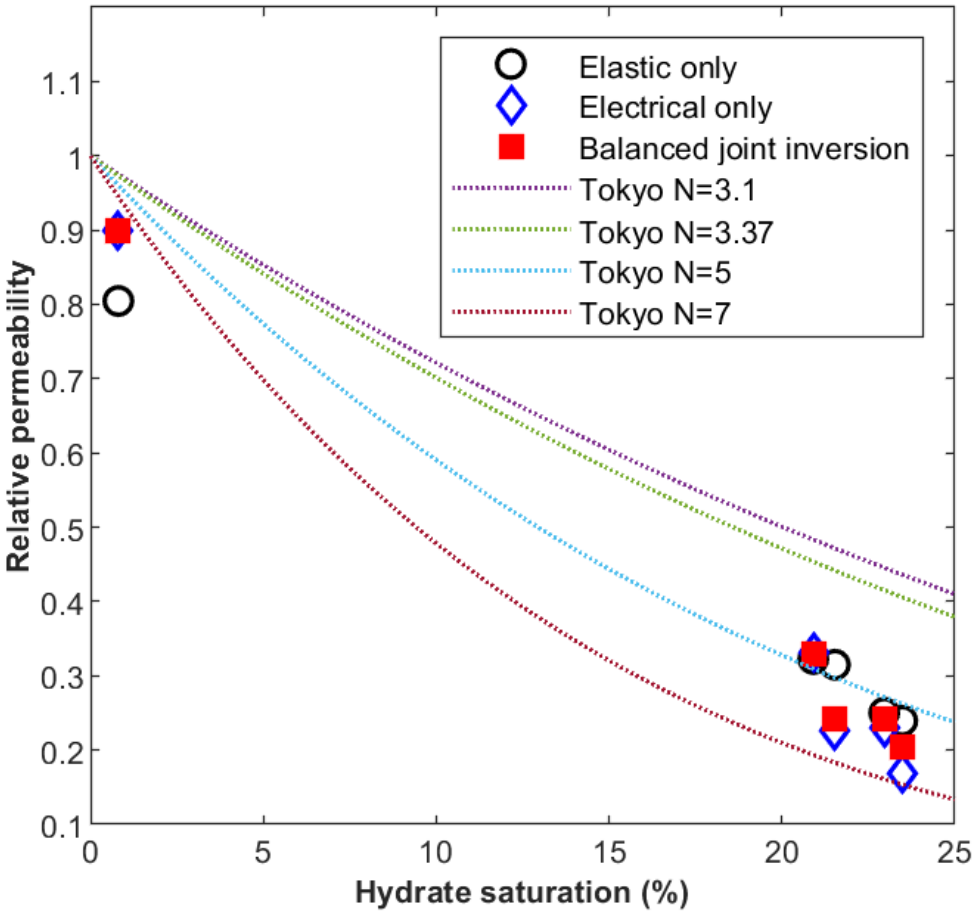

Figure 3. Relative permeability from elastic-only, electrical-only and balanced joint inversion, compared with the plotted Tokyo-model curves.

5. REFERENCES

Hauck, C., Böttcher, M., and Maurer, H. (2011). A new model for estimating subsurface ice content based on combined electrical and seismic data sets. The Cryosphere, 5, 453–468. https://doi.org/10.5194/tc-5-453-2011.

Mollaret, C., Wagner, F. M., Hilbich, C., Scapozza, C., and Hauck, C. (2020). Petrophysical joint inversion applied to Alpine permafrost field sites to image subsurface ice, water, air, and rock contents. Frontiers in Earth Science, 8, 85. https://doi.org/10.3389/feart.2020.00085.

Mathys, T., et al. (2025). Quantifying permafrost ground ice contents in the Tien Shan and Pamir: a petrophysical joint inversion approach using a geometric mean model. The Cryosphere, 19, 6591–6628. https://doi.org/10.5194/tc-19-6591-2025.

Mewes, B., Hilbich, C., Delaloye, R., and Hauck, C. (2017). Resolution capacity of geophysical monitoring regarding permafrost degradation induced by hydrological processes. The Cryosphere, 11, 2957–2974. https://doi.org/10.5194/tc-11-2957-2017.

Sahoo, S. K., Madhusudhan, B. N., Marín-Moreno, H., et al. (2018). Laboratory insights into the effect of sediment-hosted methane hydrate morphology on elastic wave

velocity from time-lapse 4-D synchrotron X-ray computed tomography. Geochemistry, Geophysics, Geosystems, 19, 4502–4521. https://doi.org/10.1029/2018GC007710.

Sahoo, S. K., Marín-Moreno, H., North, L. J., et al. (2018). Presence and consequences of coexisting methane gas with hydrate under two-phase water-hydrate stability conditions. Journal of Geophysical Research: Solid Earth, 123, 3377–3390. https://doi.org/10.1029/2018JB015598.

Sahoo, S. K., and Best, A. I. (2021). The influence of gas hydrate morphology on reservoir permeability and geophysical shear wave remote sensing. Journal of Geophysical Research: Solid Earth, 126, e2021JB022206. https://doi.org/10.1029/2021JB022206.

Wagner, F. M., Mollaret, C., Günther, T., Kemna, A., and Hauck, C. (2019). Quantitative imaging of water, ice and air in permafrost systems through petrophysical joint inversion of seismic refraction and electrical resistivity data. Geophysical Journal International, 219, 1866–1875. https://doi.org/10.1093/gji/ggz402.